# Phase-resolved polarization sensitive optical coherence tomography imaging of tendon and muscle

Hongwu Ren, Yimin Wang, Zhihua Ding, Yonghua Zhao, J. Stuart Nelson, Zhongping Chen

Beckman Laser Institute and the Center for Biomedical Engineering
University of California, Irvine, California 92612

## ABSTRACT

We describe a phase-resolved polarization sensitive optical coherence tomography system that can obtain the Stokes vectors, polarization diversity intensity, and birefringence images of rat-tail tendon and muscle. The Stokes vectors were obtained by processing the analytical interference fringe signals from two perpendicular polarization-detection channels for the same reference polarization state. From the four Stokes vectors, the birefringence image, which is insensitive to orientation of the optical axis in the sample, and the polarization diversity intensity image, in which speckle noise is greatly reduced, were obtained. The birefringence changes in the rat muscle caused by freezing were investigated using phase-resolved polarization sensitive optical coherence tomography. It was found that freezing degrades birefringence in rat muscle.

**Keywords**: optical coherence tomography, polarization sensitive optical coherence tomography, phase-resolved, rat-tail tendon, rat muscle, freezing and birefringence.

## 1. INTRODUCTION

Optical coherence tomography (OCT) is a noninvasive, noncontact imaging modality that can provide micrometer-scale cross-sectional images of tissue microstructure [1]. OCT was first used clinically in ophthalmology for the imaging and diagnosis of retinal disease. Recently, OCT has been applied to imaging subsurface structure in human skin, blood vessels, oral cavity, and the respiratory, urogenital, and gastrointestinal tracts [2].

Several alternative modalities based on OCT technology have been developed for imaging changes in tissue physiology function. Among them, optical Doppler tomography (ODT) and polarization sensitive optical coherence tomography (PS-OCT) have been developed and widely applied to functional imaging of tissue. ODT combines the Doppler principle with coherence gating for tomographic imaging of tissue microstructure and blood flow simultaneously [3-9]. PS-OCT combines polarization detection with OCT to determine tissue birefringence [10-17]. Both techniques use the phase information from the interference fringes to obtain additional physiologically important information [5-9, 12-16]. PS-OCT has been used to image the retina [12] and burn depth in skin [14-15]. Moreover ODT and PS-OCT modules have been combined together to image human skin [18-19].

## 2. METHODS

### 2.1 Phase-resolved PS-OCT setup and trigger relationship

We describe a phase-resolved PS-OCT system that can obtain the Stokes vectors, polarization diversity intensity and birefringence images of rat-tail tendon and muscle. The system is based on a phase-resolved signal processing method, from which the microstructure and birefringence information were obtained by processing the analytical interference fringe signals derived from two perpendicular polarization-detection channels. The fiber-based high-speed PS-OCT



Coherence Domain Optical Methods and Optical Coherence Tomography in Biomedicine VII,
Valery V. Tuchin, Joseph A. Izatt, James G. Fujimoto, Editors, Proceedings of SPIE
Vol. 4956 (2003) © 2003 SPIE · 1605-7422/03/$15.00

system is shown in Figure 1. A 1310 nm partially coherent light source (AFC Technologies) with a FWHM bandwidth of 80 nm was used as the light source. Light entering a 2x2 fiber splitter is divided equally into sample and reference arms of the Michelson interferometer. In the reference arm, a rapid scanning optical delay (RSOD) line [20-21] is aligned such that only group delay scanning at 500 Hz is generated without phase modulation. A stable ramp phase modulation at 500 kHz is generated using an E-O modulator for heterodyne detection. When light returned from the RSOD passes through the phase modulator, it polarizes light to 45° with respect to the optical axis of the crystal in the polarization modulator. A probe with a collimator and infinity-corrected objective driven by a translation stage is employed in the sample arm. The fringe signals from the two polarization channels are detected by two photo-detectors, then high pass filtered, amplified and digitized by a 12-bit analogue to digital conversion board (dual-channel, 5M samples/s per channel, National Instruments). A polarization modulator is used to control the polarization state of light in the reference arm, which rapidly varied between states orthogonal in the Poincaré sphere at 500 Hz. The choice of orthogonal polarization states in the Poincaré sphere is important because it ensures that the birefringence measurements will be independent of the orientation of the optical axis in the sample. In order to measure the Stokes vectors accurately, four states of light polarization are generated for each lateral pixel [13-14]. For each polarization state, one A-line scan is performed. Therefore, a total of four A-line scans are used to calculate the Stokes vectors, polarization diversity intensity and birefringence images simultaneously in one program module for one lateral pixel. The synchronizing time clock diagram is shown in Figure 2. The positive slope of the signal in channel 4 acts as a trigger to start the phase modulation signal generation and data acquisition. The negative slope acts as a trigger to stop the phase modulation signal generation and data acquisition. The negative slope of this signal triggers the start of polarization modulation signal generation. The data acquisition (DAQ) is ready to start when the trigger out signal in channel 1 has a negative slope. Channel 3 is the triangle signal driving the galvanometer scanner. The driving signals for the polarization state modulator, phase modulator and galvanometer scanner are all generated by GPIB synthesis using three function generators. The translation stage is controlled by the GPIB so that it moves one pixel when the polarization modulation signal in channel 2 has run four steps.

### 2.2 Phase-resolved signal processing for PS-OCT

To extract phase information from the detected signal, we first calculate the complex analytical signal $\tilde{\Gamma}(t)$ of the interference fringe using a Hilbert transform [5]:

$$\tilde{\Gamma}(t) = \Gamma(t) + \frac{i}{\pi} P\int_{-\infty}^{\infty} \frac{\Gamma(t')}{t'-t} dt' \tag{1}$$

Where $i$ is the imaginary symbol and $P$ denotes the Cauchy principle value. Because the interference signal Γ(t) is quasi-monochromatic, the complex analytical signal is given by:

$$\tilde{\Gamma}(t) = 2\int_{0}^{+\infty}\int_{-T}^{+T} \Gamma(t')\exp(-2\pi i v t')dt'\exp(2\pi i v t)dv \tag{2}$$

The digital approach to determine the complex analytical signal using Hilbert transformation is shown in the following block diagram [7,19]

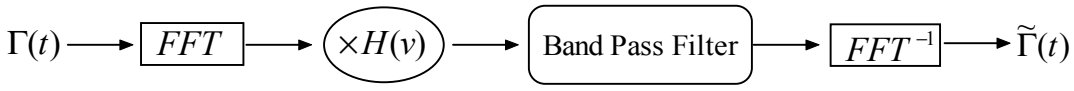


where FFT denotes the fast Fourier transform, × is a multiplying symbol, and $H(\nu)$ is the Heaviside function given by:

$$H(v) = \begin{cases} 0 & v < 0 \\ 1 & v \geq 0 \end{cases} \tag{3}$$

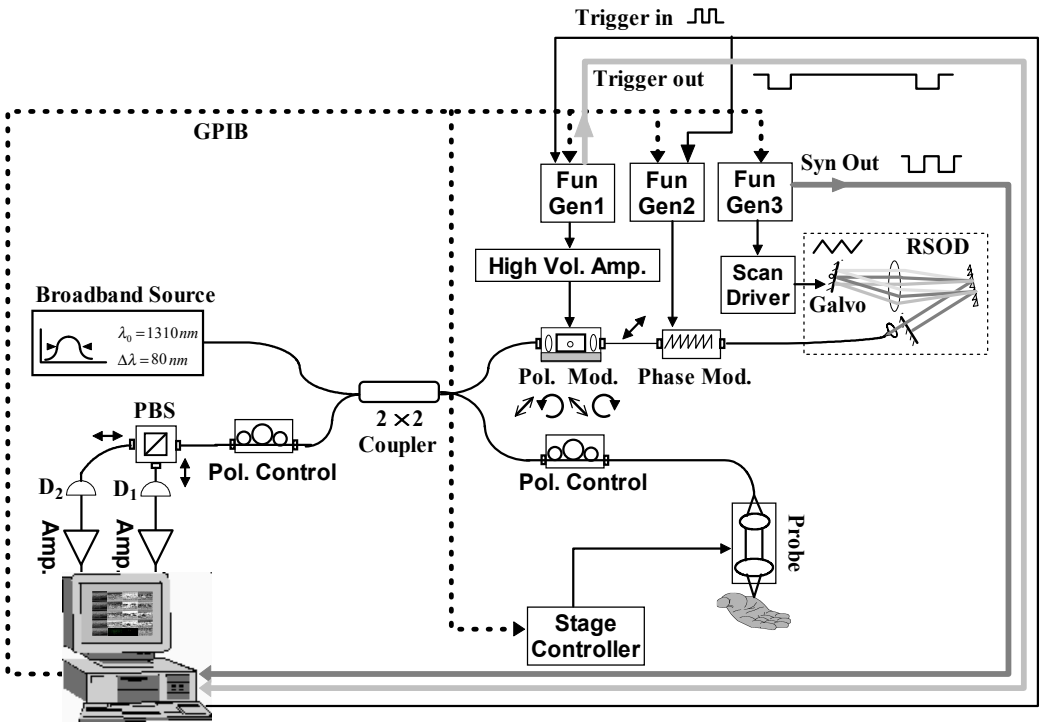


Figure 1. Fiber-based PS-OCT system. Pol. Mod. : polarization state modulator, Pol. Control: polarization controller, Phase Mod.: phase modulator, PBS: polarization beam splitter, RSOD: rapid scanning optical delay line, $D_1$, $D_2$: detectors. Galvo: galvanometer scanner, High Vol. Amp.: high voltage amplifier, Fun Gen1, Fun Gen2, Fun Gen3 : function generators, GPIB: general purpose interface bus, Syn. Out: synchronizing signal of the driving signal for galvanometer scanner, which is from Fun Gen3, Trigger in: trigger in signal to Fun Gen1, Fun Gen2, which is generated from the National Instruments (NI) DAQ board, Trigger out: trigger out signal from Fun Gen1 to the DAQ board for arming the DAQ. Amp.: low noise preamplifier.

and FFT $^{-1}$ denotes the inverse fast Fourier transform. Multiplication of the Heaviside function is equivalent to performing an operation that discards the spectrum in the negative frequency region.

For every polarization state controlled by the polarization modulator, the A-scan signals corresponding to the two orthogonal polarization diversity channels were digitized. Considering the quasi-monochromatic nature of the light, the coherence matrix can be calculated from the complex electrical field vector from these two channels [22]:

$$J = \begin{bmatrix} \left\langle E_H^*(t)E_H(t)\right\rangle & \left\langle E_H^*(t)E_V(t)\right\rangle \\ \left\langle E_V^*(t)E_H(t)\right\rangle & \left\langle E_V^*(t)E_V(t)\right\rangle \end{bmatrix} = \begin{bmatrix} J_{HH} & J_{HV} \\ J_{VH} & J_{VV} \end{bmatrix} \tag{4}$$

where $E_H, E_V$ are the components of the complex electric field vector corresponding to the horizontal and vertical polarization channels, respectively, and $E_H^*, E_V^*$ are their conjugates, respectively. The Stokes vector can be derived from the coherence matrix [22]:

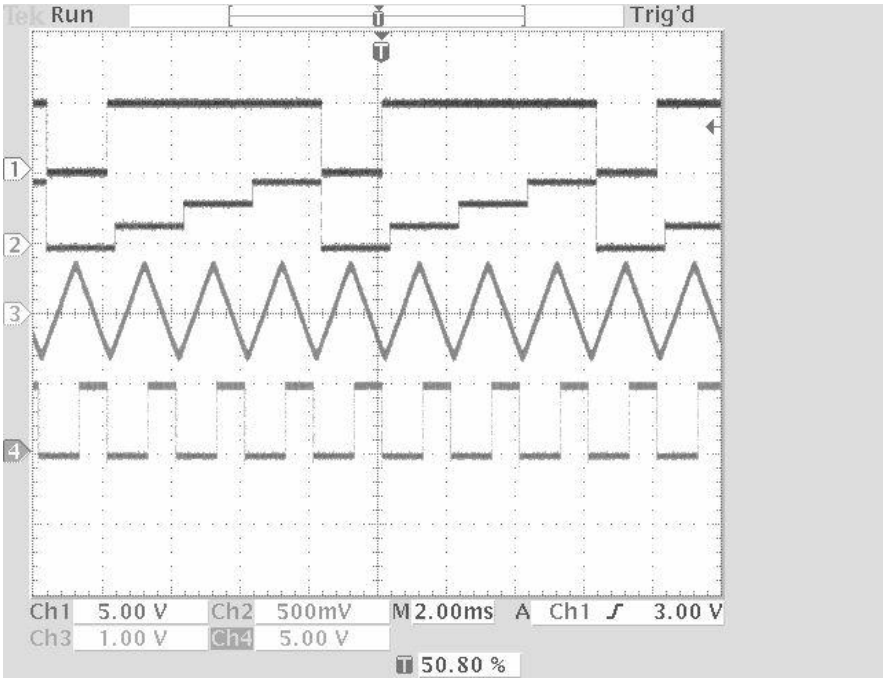


Figure 2. Synchronizing time clock diagram for the PS-OCT system. Channel 1 is the signal generated from the synchronized trigger output of Function Generator 1, and arms the A/D conversion. Channel 2 is the signal generated by Function Generator 1 to control the polarization modulator. Channel 3 is the triangle signal from the Function generator 3 to control the galvanometer scanning. Channel 4, which is the trigger in signal in Figure 1, is the signal generated by synchronized output of Function Generator 3 through a digital delay, it is used to trigger the phase modulation and data acquisition.

$$\begin{aligned} S_0 &= J_{HH} + J_{VV} \\ S_1 &= J_{HH} - J_{VV} \\ S_2 &= J_{HV} + J_{VH} \\ S_3 &= i\left(J_{VH} - J_{HV}\right) \end{aligned} \tag{5}$$

where $S_0$, $S_1$, $S_2$, and $S_3$ are the four components of the Stokes vector. $S_1$, $S_2$, and $S_3$ are the coordinates of the Stokes vector in the Poincar sphere characterizing the polarization state of the backscattered light, and $S_0$ is the module of the Stokes vector characterizing light intensity. The Stokes vector for the *n*th pixel in the axial direction and one state of light polarization can be calculated as [19]:

$$
\begin{aligned}
S_{0,n} &= \sum_{m=n-M/2}^{m=n+M/2} \left[\tilde{\Gamma}^{H}(t_m)\tilde{\Gamma}^{H*}(t_m) + \tilde{\Gamma}^{V}(t_m)\tilde{\Gamma}^{V*}(t_m)\right] \\
S_{1,n} &= \frac{1}{S_{0,n}} * \sum_{m=n-M/2}^{m=n+M/2} \left[\tilde{\Gamma}^{H}(t_m)\tilde{\Gamma}^{H*}(t_m) - \tilde{\Gamma}^{V}(t_m)\tilde{\Gamma}^{V*}(t_m)\right] \\
S_{2,n} &= \frac{1}{S_{0,n}} * \sum_{m=n-M/2}^{m=n+M/2} 2\,\mathrm{Re}\left(\tilde{\Gamma}^{H*}(t_m)\tilde{\Gamma}^{V}(t_m)\right) \\
S_{3,n} &= \frac{1}{S_{0,n}} * \sum_{m=n-M/2}^{m=n+M/2} 2\,\mathrm{Im}\left(\tilde{\Gamma}^{H*}(t_m)\tilde{\Gamma}^{V}(t_m)\right)
\end{aligned}
\tag{6}
$$

where $M$ is an even integer number that determines the window size in the axial direction, $\tilde{\Gamma}^{H}(t_m)$ and $\tilde{\Gamma}^{V}(t_m)$ are the complex signals detected from the two orthogonal polarization channels at axial time $t_m$, $\tilde{\Gamma}^{H*}(t_m)$ and $\tilde{\Gamma}^{V*}(t_m)$ are their conjugates. From the Stokes vectors for the four states of light polarization, the polarization diversity intensity image is obtained by averaging the four $S_0$ images. The birefringence image is calculated by rotation of the Stokes vectors in the Poincar sphere [13-14].

## 3. RESULTS

We have used our phase-resolved PS-OCT system to perform imaging of rat-tail tendon and muscle. The simultaneous Stokes vectors, polarization diversity intensity, and birefringence images of rat-tail tendon in the axial direction are shown in Figure 3. The imaged area is 5 x 1.28 mm. For the Stokes vectors image in Figure 3(1), from left to right, they are $S_0$, $S_1$, $S_2$, and $S_3$, respectively, from top to bottom the polarization state is changed as shown in the figure: 45° linear, left rotate circular, 135°, right rotate circular. Polarization diversity intensity and birefringence images are shown in Figure 3(2) and Figure 3(3) respectively. The simultaneous Stokes vectors, polarization diversity intensity, and birefringence images of rat-tail tendon in the cross-sectional direction are shown in Figure 4. The imaged area is 5 x 2.04 mm. Implementation of the polarization diversity detection in the intensity image significantly reduces the artifact due to tissue birefringence. Moreover, speckle noise is also greatly reduced. The clear-banded structure in the birefringence image identified by PS-OCT indicates the tissue birefringence distribution in the rat-tail tendon. We also used our PS-OCT system for studying the progressive degradation of birefringence in rat muscle after tissue freezing for two and eight hours at – 4 C°, as shown in Figures 5-7. The imaged area is 5 x 2.04 mm. The period of the banded structure in the birefringence image shown in Figure 6(3), is increased, when compared to the birefringence image of fresh rat muscle, shown in Figure 5(3). This indicates that the birefringence is reduced after freezing the rat muscle for two hours. The period of the banded structure in the birefringence image shown in Figure 7(3), when compared to Figure 5(3) and Figure 6(3), disappears due to the degradation of the tissue. This indicates that the birefringence in the rat muscle degrades after freezing for eight hours.

## 4. CONCLUSION

In summary, we have developed a phase-resolved PS-OCT system capable of simultaneous imaging of the Stokes vectors, polarization diversity intensity, and birefringence. The detection scheme we implemented allows polarization diversity averaging in the detection of intensity, which greatly reduces the influence of speckle noise and tissue birefringence artifact. Phase-resolved PS-OCT that can simultaneously provide tissue structure and birefringence information has great potential for both basic biomedical research and clinical applications.

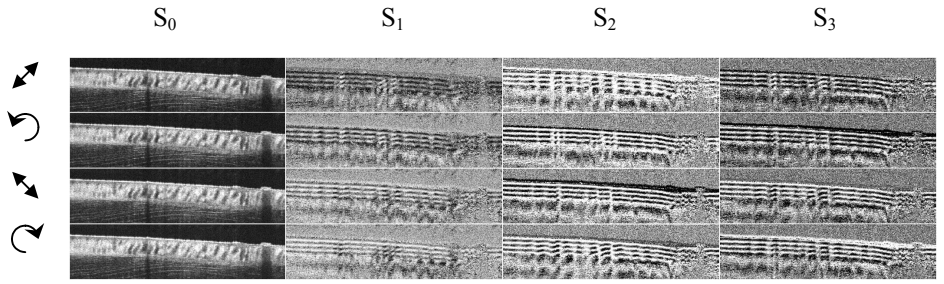


(1) Stokes vectors image

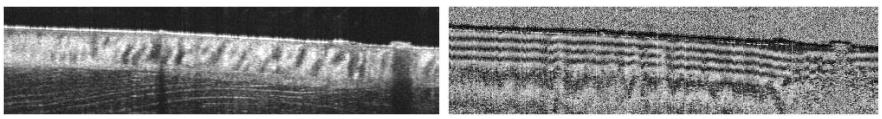

(2) Polarization diversity intensity image

(3) Birefringence image

Figure 3. Simultaneous imaging of the Stokes vectors, polarization diversity intensity, and birefringence in rat-tail tendon in the axial direction.

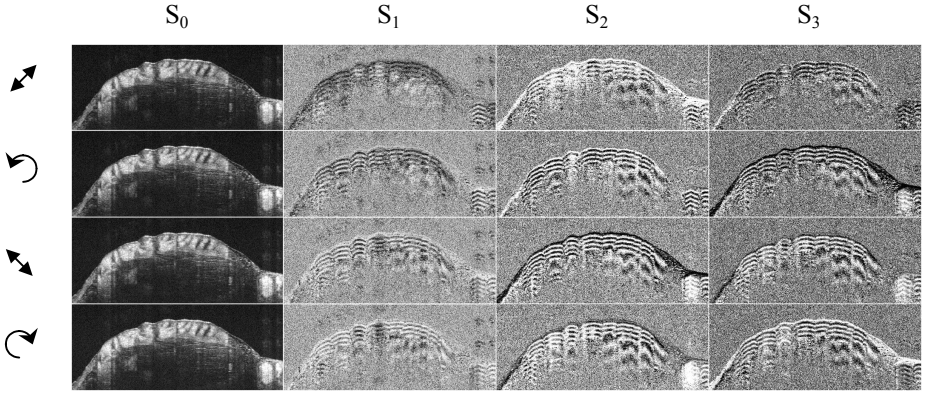


(1) Stokes vectors image

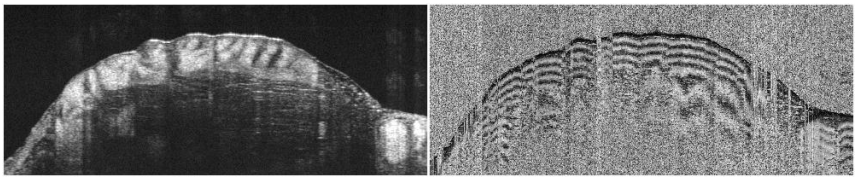

(2) Polarization diversity intensity image

(3) Birefringence image

Figure 4. Simultaneous imaging of the Stokes vectors, polarization diversity intensity, and birefringence in rat-tail tendon in the cross sectional direction.

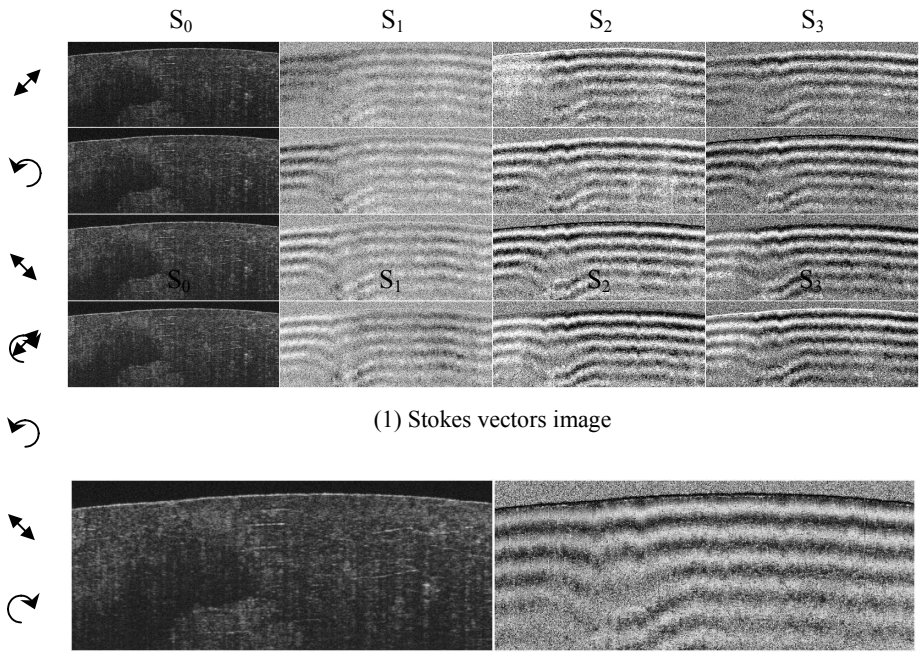


Figure 5. Simultaneous imaging of the Stokes vectors, polarization diversity intensity, and birefringence in fresh rat muscle.

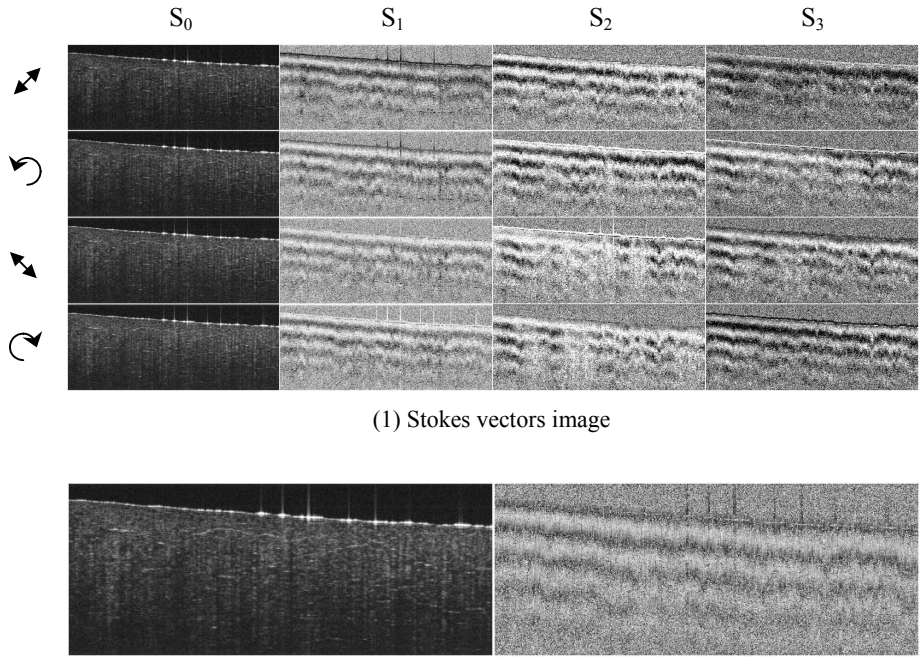


Figure 6. Simultaneous imaging of the Stokes vectors, polarization diversity intensity, birefringence in rat muscle frozen for two hours.

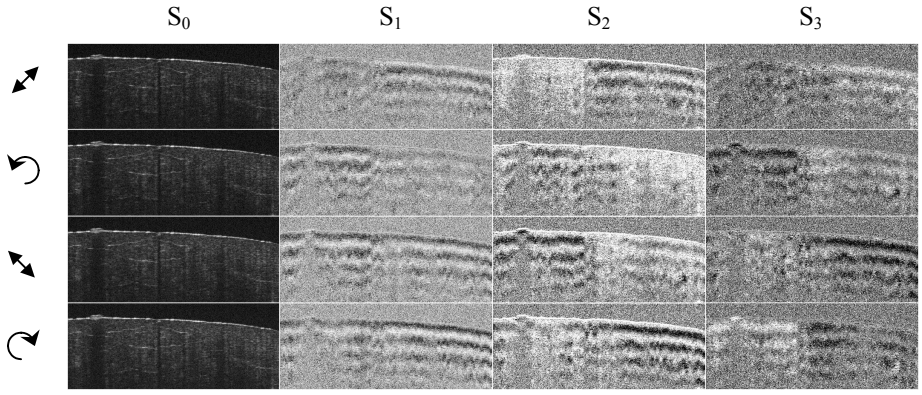


(1) Stokes vectors image

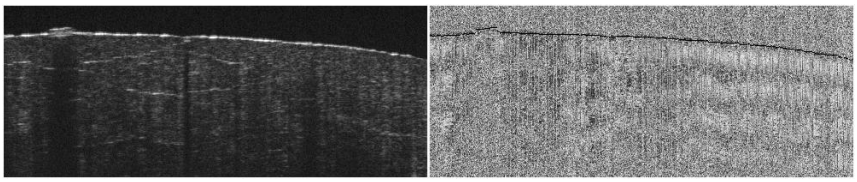

(2) Polarization diversity intensity image (3) Birefringence image

Figure 7. Simultaneous imaging of the Stokes vectors, polarization diversity intensity, and birefringence in rat muscle frozen for eight hours.

## ACKNOWLEGEMENTS

This work was supported by research grants awarded from the National Institutes of Health (EB-00293, RR-01192 and EB-00255) and National Science Foundation (BES-86924). Institutional support from the Air Force Office of Scientific Research (F49620-00-1-0371), and the Beckman Laser Institute Endowment is also gratefully acknowledged.

## REFERENCES

1. D. Huang, E. A. Swanson, C. P. Lin, J. S. Schuman, W. G. Stinson, W. Chang, M. R. Hee, T. Flotte, K. Gregory, C. A. Puliafito and J. G. Fujimoto, "Optical coherence tomography," Science 254, 1178-1181 (1991).
2. B. E. Bouma, G. J. Tearney, "*Handbook of optical coherence tomography*," (Marcel Derker, Inc. New York 2002).
3. Z. Chen, T. E. Milner, S. Srinivas, X. Wang, A. Malekafzali, M. J. C. van Gemert and J. S. Nelson, "Noninvasive imaging of *in vivo* blood flow velocity using optical Doppler tomography," Opt. Lett. 22, 1119-1121 (1997).
4. J. A. Izatt, M. D. Kulkarni, S. Yazdanfar, J. K. Barton, and A. J. Welch, " *In vivo* bidirectional color Doppler flow imaging of picoliter blood volumes using optical coherence tomography," Opt. Lett. 22,1439-1441 (1997).

5. Y. Zhao, Z. Chen, C. Saxer, S. Xiang, J. F. de Boer and J. S. Nelson, " Phase-resolved optical coherence tomography and optical Doppler tomography for imaging blood flow in human skin with fast scanning speed and high velocity sensitivity," Opt. Lett. 25, 114-116 (2000).
6. J.S. Nelson, K.M. Kelly, Y. Zhao, Z. Chen, "Imaging blood flow in human port-wine stain in situ and in real time using optical Doppler tomography," Arch Dermatol, 137, 741-744 (2001)
7. Z. Ding, Y. Zhao, H. Ren, J. S. Nelson, Z. Chen, "Real-time phase-resolved optical coherence tomography and optical Doppler tomography," Opt. Express, 10, 236-245 (2002)
8. V. Westphal, S. Yazdanfar, A. M. Rollins, J. A. Izatt, "Real-time, high velocity-resolution color Doppler optical coherence tomography," Opt. Lett, 27, 34-36 (2002).
9. H. Ren, K. M. Brecke, Z. Ding, Y. Zhao, J. S. Nelson, Z. Chen, "Imaging and quantifying transverse flow velocity with the Doppler bandwidth in a phase-resolved functional optical coherence tomography," Opt. Lett., 27, 409-411 (2002).
10. J. F. de Boer, Z. Chen, J. S. Nelson, S. M. Srinivas, A. Malekafzali, " Imaging thermally damaged tissue by polarization sensitive optical coherence tomography," Opt. Express, 3, 212-218 (1998).
11. M. J. Everett, K. Schoenenberger, B.W. Colston, L.B.Da Silva, "Birefringence characterization of biological tissue by use of optical coherence tomography," Opt. Lett. 23, 228-230 (1998).
12. M. G. Ducros, J. D. Marsack, H.G. Rylander, S. L. Thomsen, T.E. Milner, "Primate retina imaging with polarization-sensitive optical coherence tomography," J. Opt. Soc. Am. A, 18, 2945-2956 (2001).
13. E. Saxer, J. F. de Boer, B. H. Park, Y. Zhao, Z. Chen, J. S. Nelson, " High-speed fiber based polarization-sensitive optical coherence tomography of in vivo human skin," Opt. Lett. 25, 1355-1357 (2000).
14. H. Park, J. F. de Boer C. Saxer, S. M. Srinivas, H. L. Huang, Q. Ngo, Z. Chen, J.S. Nelson, "Burn depth determination by high-speed fiber-based polarization sensitive optical coherence tomography at 1.3 micrometers," SPIE 3915, 243-248 (2000).
15. B.H. Park, C. Saxer, S.M. Srinivas, J. S. Nelson, J.F. de Boer, **"**In vivo burn depth determination by high-speed fiber-based polarization sensitive optical coherence tomography," J. Biomed.Opt. 6, 474-479 (2001).
16. C. Hitzenberger, E. Goetzinger, M. Sticker, M. Pircher, A. Fercher, " Measurement and imaging of birefringence and optical axis orientation by phase resolved polarization sensitive optical coherence tomography," Opt. Express, 10, 780-790 (2001).
17. J. E. Roth, J. A. Kozak, S. Yazdanfar, A. M. Rollins, J. A. Izatt, "Simplified method for polarization-sensitive optical coherence tomography," Opt. Lett. 14, 1069-1071 (2001).
18. M. C. Pierce, B. H. Park, B. Cense, M.S. Shishkov, J. F. de Boer, "Simultaneous intensity, birefringence, and flow measurement using high-speed fiber-based optical coherence tomography," SPIE, 4619, 171-1799 (2002).
19. H. Ren, Z. Ding, Y. Zhao, J. S. Nelson, Z. Chen, "Phase-resolved functional optical coherence tomography: simultaneous *in situ* imaging of the Stokes vectors, polarization diversity intensity, blood flow velocity, standard deviation, and birefringence in human skin," Opt. Lett. 27, 1702-1704 (2002).
20. J. Tearney, B. E. Bouma and J. G. Fujimoto, "High-speed phase- and group-delay scanning with a grating-based phase controldelay line," Opt. Lett. 22, 1811-1883 (1997).
21. M. Rollins, M. D. Kulkarni, S. Yazdanfar, R. Ung-arunyawee and J. A. Izatt, "In vivo video rate optical coherence tomography," Opt. Express, 3, 219-229 (1998).
22. L. Mandel and E. Wolf, *Optical coherence and quantum optics* (Cambridge University Press, Cambridge, England, 1995). Chap.6.